ACS APPLIED ENERGY MATERIALS

Cite This: ACS Appl. Energy Mater. 2018, 1, 1146−1157

Article

www.acsaem.org

Prediction of the Effective Thermal Conductivity of Hollow Sphere Foams

Zian Jia, Zhen Wang, David Hwang, and Lifeng Wang*

Department of Mechanical Engineering, State University of New York at Stony Brook, Stony Brook, New York 11794, United States

Supporting Information

ABSTRACT: Microscale and mesoscale hollow sphere foam (HSF) materials have attracted tremendous attention in recent decades due to their potential applications. Here, we study the effective thermal conductivity (ETC) of HSFs using an equivalent model, in which hollow spheres are first treated as equivalent solid particles, and then are combined with the ETC models that have been previously developed for solid particle filled composites. Compared with the rule of mixture model and syntactic foam models, this model shows better accuracy in predicting the ETC of HSFs. The theoretical model, together with finite element simulations, is then used to guide the design of HSFs. The results show that smaller size (nanoscale), lower packing fraction, lower shell conductivity, larger shell porosity, longer binder length, and higher interfacial thermal resistance lead to significantly lower ETC, while packing pattern, sphere size distribution, pore size of the porous shell, and binder radius have relatively minor influences. Moreover, size effects are investigated to use the proposed model for microscale and nanoscale problems. Aside from the well-known Knudsen effect, the size effect induced by interfacial thermal resistance should also be considered when the sphere size is smaller than a critical length. Interestingly, the Knudsen effect in the pores of a porous shell is shown to have an insignificant influence on the ETC. This study provides deep understanding of the thermal (and electrical, equivalently) behavior of the HSFs, which will potentially aid future design of novel and multifunctional HSF materials.

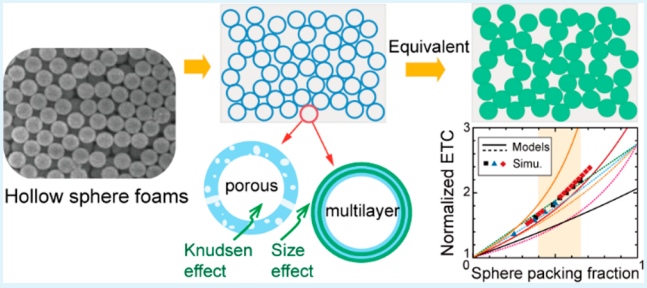

KEYWORDS: *hollow sphere foams, mesoscale hollow-structured material, effective thermal conductivity, porous shell, multilayer shell, size effect*

1. INTRODUCTION

Hollow sphere foam (HSF) material is a class of cellular solids that exhibit low density, large void space, and large specific surface area, which offer great potential for novel mechanical, physical, and chemical applications at different length scales. Traditionally, macroscale (millimeter scale or larger) HSFs are widely used in applications like energy absorption,[1,2] thermal management,[3] fluid permeability control,[4] and ultrasensitivity sensors.[5,6] In recent decades, synthetic approaches based on microscale and mesoscale removable templates[7,8] have enabled the manufacture of hollow spheres with various materials and sizes ranging from micrometer to nanometer.[9−14] The synthesized hollow spheres are then assembled into relatively defect-free foam materials with a binding,[9] sintering,[10] or self-assembling process[15−19] (Figure 1 shows two typical HSFs). Moreover, methods such as surfactant-templating[20] and interfacial reactions[21] enable the synthesis of hollow spheres with porous shells,[22] while synthetic strategies like lost wax approach[23] and layer by layer assembly method[24] enable the formation of foams with a multilayer shell.[25,26] The great advances in synthesis technology have enabled various microscale applications of HSFs such as confined catalyst supports,[27−29] photonic crystals,[30,31] drug storage/delivery nanocontainers,[22,32] and multilayer shell supercapacitors.[25,26]

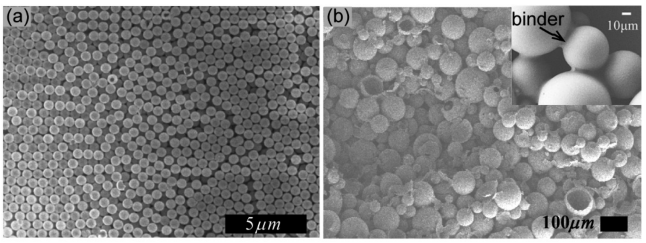

Figure 1. Typical microscale HSFs. (a) SEM image of orderly arranged monosized hollow silica nanoparticles, showing the transition from dilute sphere filling (left) to dense sphere filling (right). Reproduced with permission from ref 18. Copyright 2012 American Chemical Society. (b) SEM image of hollow spheres with size distribution (average diameter ∼65 μm). The spheres are assembled with minimum contact binding; the inset shows the binder between hollow spheres. Reproduced with permission from ref 9. Copyright 2017 Springer Nature.

Received: December 12, 2017
Accepted: February 26, 2018
Published: February 26, 2018

DOI: 10.1021/acsaem.7b00264
ACS Appl. Energy Mater. 2018, 1, 1146−1157

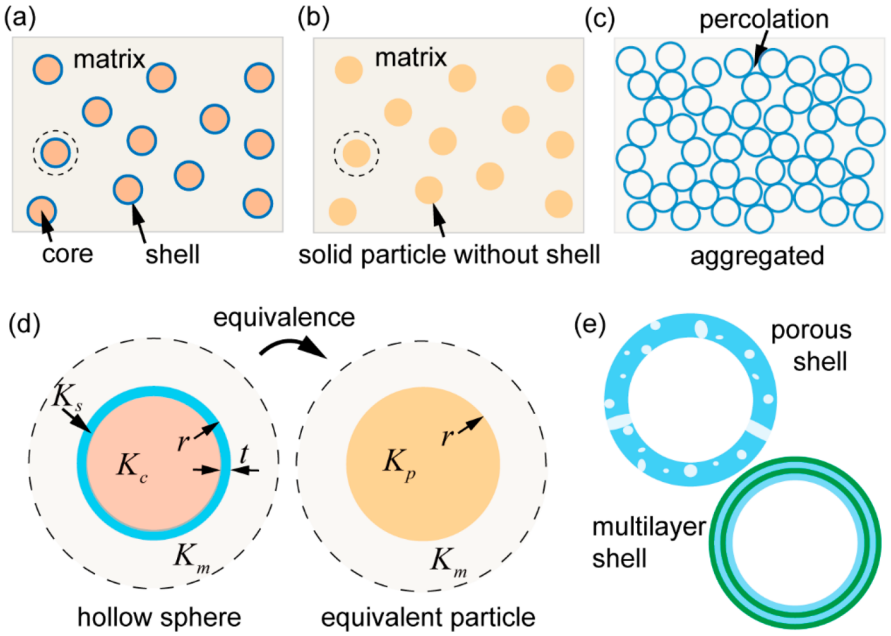

Figure 2. Schematics of hollow sphere and solid particle filled composites. (a) Hollow sphere filled composite with three phases, the matrix, the core, and the shell. (b) Solid particle filled composite with particle distribution equivalent to part a. (c) Hollow sphere foam is a special case of hollow sphere filled composites where both the matrix and core materials are air, and the spheres are aggregated together ensuring self-support of the foam. (d) The equivalence of a hollow sphere as a solid "equivalent particle". The outer radius of the sphere is r; the thickness of the shell is t. K_m, K_c, and K_s are the conductivity of the matrix, the core, and the shell, respectively, and K_p is the conductivity of the equivalent particle. (e) Two special types of shells are widely adopted in multifunctional HSF designs: porous shell (top) and multilayer shell (bottom).

Compared to the huge technological leap in the synthesis and applications of microscale HSFs, the study of their thermal, mechanical, and electrical properties has lagged behind.

In HSF applications such as thermal insulation or catalyst supports, or when the cooling/heating rate should be finely controlled, the heat transfer in HSFs is of great interest. The thermal behavior of heterogeneous materials (e.g., composites, foams) can be evaluated with effective thermal conductivity (ETC), by which heterogeneous materials are treated as homogeneous materials. The earliest effort in finding the ETC of heterogeneous materials dates back to Maxwell[33] and Lord Rayleigh,[34] who have obtained the ETC of solid particle filled composites by equalizing the far-field temperature distribution of the composite to an effective medium, which is known as the effective medium theory. Bruggeman and Landauer[35] have developed another approach to predict the ETC by incrementally introducing infinitesimal changes to the matrix material. Their model is more accurate for high filler volume fractions, but the ETC is given implicitly, which is not desirable. Later on, Benveniste[36] and Hasselman and Johnson[37] have independently taken the interfacial thermal resistance (ITR) into consideration. Nan[38] has introduced an ETC model for predicting the thermal conductivity of arbitrary particulate composites based on the multiple-scattering approach. There have been many other efforts, for which references 39−41 provide a comprehensive review. Aside from these theoretical studies, numerical methods have also been developed to study the ECT of composite materials including the effective unit cell approach,[42] finite element simulation,[43,44] and lattice Boltzmann method.[45,46]

While all the above ETC models are developed for solid particle filled composites, reports on the HSFs are relatively limited, especially for microsized and nanosized foams. Fiedler et al.[47] have studied the effect of solid material fraction on the ETC of macroscale sintered hollow metallic foams, and Liang and Li[48] have experimentally measured the thermal insulation property of a hollow glass bead filled composite polymer. More recently, Thiele et al.[49] have combined numerical simulation and Felske's model[50] to predict the ETC of spherical mono- and polydispersed core−shell particles, showing that ETC is independent of the spatial distribution of spheres. Pal,[51] Profiri,[52] and Park[53] have also developed models that accurately predict the ETC of syntactic foams, which are reviewed in ref 54. In addition, discussion of metallic HSFs with multifunctional applications can be found in ref 55. These studies have laid a solid foundation for predicting the ETC of HSFs. However, the syntactic foam models are not accurate for HSFs with high packing fractions, and the study on modeling nanoscale HSFs is relatively limited. To the best of our knowledge, the ETC of HSFs with porous shell and multilayer shell and the size effects have not been studied systematically.[22]

In this paper, we evaluate the ETC of HSFs by transferring the hollow sphere foam problems into traditional solid particle filled problems using Nan's theoretical equivalence,[29,43] which enables us to use all the previously developed ETC theories of solid particle filled composites. The theoretical models are verified by numerical simulations and then used to study the effect of sphere size, ITR, and porous shell and multilayered shell, providing guidelines for the design of microscale HSFs. Furthermore, the effects of sphere size distribution and binder shape are also investigated with combined numerical simulation and theoretical modeling. Finally, the relation between the effective thermal conductivity and the effective Young's modulus is plotted in a material property chart to examine the design space of HSFs.

DOI: 10.1021/acsaem.7b00264
ACS Appl. Energy Mater. 2018, 1, 1146−1157

2. MATERIALS AND METHODS

To evaluate the ETC of HSFs, we first consider a hollow sphere filled composite with three phases, namely, the matrix, the shell, and the core (Figure 2a). For simplicity, the spheres are first assumed to be monosized. Knowing that the ETC models for solid particle filled composites (Figure 2b) have been well-developed, a very straightforward way to calculate the ETC of the hollow sphere filled composites is by transferring the hollow sphere problems (Figure 2a) to solid particle problems (Figure 2b), as depicted in Figure 2d. Then, the key is to find the equivalence relation between a hollow sphere and an equivalent solid particle, as will be discussed in Section 2.1. Note that the HSFs can be regarded as hollow sphere filled composites, where both the matrix and the core material are air (Figure 2c).

Generally, three heat transfer modes contribute to the total effective thermal conductivity of HSFs, namely, heat convection, heat conduction, and heat radiation. Heat convection mediated by fluid flow is insignificant when the Rayleigh number is smaller than 1000.[11] For most HSFs (sphere radius <20 mm in air), this condition is satisfied.[11] On the other hand, thermal radiation can be estimated using the unit cell method[40] as $K^r = 8F_E^*\sigma r\overline{T}^3$, where $\overline{T}$ is the mean temperature, σ is the Stefan−Boltzmann constant, F_E^* is radiation exchange factor $[F_E^* = 1/(P^{-1} - 1)]$, and P is porosity. For porous materials $F_E^* = 0.2-0.6$, when cell radius $r \sim 100$ μm, $\overline{T} \sim 300$ K, K^r is estimated as $0.8-2.4 \times 10^{-4}$ W/m K. Except for HSFs with extremely low ETC (e.g., aerogel), or unless the material is used at very high temperatures, radiation will not play a significant role. For most mesoscale foams, K^r is a relative small amount, therefore, only thermal conduction is discussed in this study.

2.1. Equivalence between a Hollow Sphere and a Solid Particle. To find the equivalence relation, consider a hollow sphere with outer radius r, core conductivity K_c surrounded by a shell of thickness t and conductivity K_s, sitting in a matrix of conductivity K_m (Figure 2d). The solid "equivalent particle" is assumed to have conductivity of K_p and radius r, surrounded by matrix of conductivity K_m. It turns out that this equivalence relation has been previously derived on the basis of the effective medium theory[38,56] (see Supporting Information), which is

$$K_p = \frac{3 + (K_c/K_s - 1)(1 + 2v)}{3 + (K_c/K_s - 1)(1 - v)}K_s \tag{1}$$

where K_p is the thermal conductivity of the equivalent particle, and $v = (1 + t/r)^{-3}$ is a dimensionless geometric parameter.

Another issue that should be considered is the ITR, since temperature discontinuity might be developed at the interfaces and imperfect contacts.[57] The temperature difference across an interface can be described by the following equation[36]

$$\kappa_1\frac{\partial T_1}{\partial n} = \kappa_2\frac{\partial T_2}{\partial n} = \beta(T_1 - T_2) \tag{2}$$

where T_1, T_2 are the temperatures at two contacted surfaces; κ_1, κ_2 are the conductivities of the two materials in contact; and β is the "skin constant". Referring to the concept of Kapitza resistance, R_{Bd},[58] which is defined as the reciprocal of β[36] ($R_{Bd} = \beta^{-1}$), the ITR in this study is defined as $R_{Bd} = \lim_{t\to 0, K_s\to 0}(t/K_s)$, which is analogous to the limiting case of heat transport across a thin and poor conductivity shell.[29] Passing eq 1 to the limit of $t \to 0$ and $K_s \to 0$, and combining it with the definition of R_{Bd}, the ETC of a solid particle with ITR is (details of derivation provided in the Supporting Information)

$$K_{ITR} = \frac{K_c}{1 + \alpha K_c/K_m} \tag{3}$$

where $\alpha = R_{Bd}K_m/r$ is a dimensionless parameter indicating the strength of the ITR. The value of R_{Bd} can be calculated theoretically or measured experimentally.[57,59]

It should be pointed out that in eq 1 the normalized ETC (K_p/K_s) of the equivalent particle is independent of the matrix property K_m, which only depends on the conductivity ratio K_c/K_s and relative thickness t/r, indicating no size effect. Therefore, eq 1 is applicable to small scales when the cell size is sufficiently larger than the phonon wavelength; thus, the scattering effect is negligible (phonon wavelength 1−10 nm in silicon[60]). By contrast, when the ITR is considered, the size effect takes place because the radius r is included in the dimensionless parameter α. As such, the ETC not only depends on t/r but also depends on the value of radius r, as will be further discussed in Section 3.1. This effect together with the Knudsen effect are two size effects that should be considered in nanosized foams.

2.2. ETC of a Hollow Sphere with Interfacial Thermal Resistance. To further consider the ETC of a hollow sphere with ITR, eq 1 is combined with eq 3, which gives the normalized ETC of a hollow sphere (as an equivalent particle) with ITR as

$$K_p^{ITR}/K_m = \frac{3 + (s_c - 1)(1 + 2v)}{s_m[3 + (s_c - 1)(1 - v)] + \alpha[3 + (s_c - 1)(1 + 2v)]} \tag{4}$$

where $s_c = K_c/K_s$ and $s_m = K_m/K_s$ are conductivity ratios of the core and the matrix, respectively.

Equation 4 is the general form of ETC for composites with three material phases (K_m, K_c, K_s) and with ITR. HSF is a simplified case where the core and matrix have the same material ($K_c = K_m$, $s_c = s_m = s$); e.g., both are air. In such a two-phase composite, when the shell material has a much higher conductivity than the matrix (and the core) $K_s \gg K_m$, corresponding to $s \ll 1$, $s \ll \alpha$, the limit of eq 1 gives $K_p = 2K_s(1 - v)/(2 + v)$, while the limit of eq 4 gives $K_p^{ITC} = K_m/\alpha$. By contrast, when shell material has a much lower conductivity than the matrix $K_s \ll K_m$, corresponding to $s \gg 1$, $s \gg \alpha$, both eqs 1 and 4 give the same limit $K_p = K_p^{ITC} = K_s(1 + 2v)/(1 - v)$. This limit analysis suggests that ITR tends to have an ignorable effect for hollow spheres with extremely poor conductivity shells, while for good conductivity shells, the ITR effect is more important.

2.3. ETC Prediction of HSFs. With the derived equivalence relation eq 4, the hollow spheres are now equivalent to solid particles with K_p^{ITC}. Subsequently, all the theoretical models for solid particle filled composites can be used to predict the ETC of the hollow spheres aggregated foams. Some of the most popularly used ETC models of solid particle filled composites are listed in Table 1. The series and parallel models are often considered as the lower and upper bounds. The effective medium model, i.e., the Maxwell model, provides a good prediction for dilute filling fractions but tends to underestimate the ETC at dense fillings, in which case the inverse Maxwell model is derived by exchanging the role of particle and matrix. The Chiew and Glandt model is an improved form of the Maxwell model with higher order term corrections, and the values of fitting parameters are given in Table 1. The Benveniste model is another popular model that is based on a self-consistent scheme and is applicable to the nondilute filling case. Furthermore, the Lewis−Nielsen model covers a wide range of particle shapes and filling patterns. The shape factor A for a sphere is 1.5, and ϕ_m is the maximum filling volume fraction for a specific packing pattern.

Taking advantage of these models, the ETC of HSFs can be calculated by substituting K_p^* (in Table 1) with K_p^{ITC} (eq 4) as the equivalent particle conductivity. The various available models in the table make this method versatile, and the model that gives the best prediction for a specific problem can be chosen. In addition, some models (e.g., Chiew and Glandt model) are based on experimental data and have fitting parameters, which can be further adjusted to obtain a perfect prediction.

2.4. Finite Element Simulation. To validate the proposed theoretical model, a number of HSFs with various relative shell thicknesses and packing fractions are created. We first use three cubic symmetric Bravais lattices to mimic the isotropic thermal behavior of HSFs, which are simple-cubic (SC), body-centered-cubic (BCC), and face-centered-cubic (FCC) lattices (Figure 3a−c). Different packing fractions are then achieved by partially removing the spheres in the original packing patterns. Note that the spheres should be removed in a controlled way that keep the foams cubic symmetric and self-supported. To achieve this, we first create super-representative volume elements (RVEs) based on $2 \times 2 \times 2$ primitive unit cells of SC, BCC,

DOI: 10.1021/acsaem.7b00264
ACS Appl. Energy Mater. 2018, 1, 1146−1157

Table 1. List of the ETC Models for Solid Particle Filled Composites

model	equation for ETC prediction
series model	$\frac{K_{eff}}{K_m} = \frac{K_p^*/K_m}{K_p^*/K_m + \phi(1 - K_p^*/K_m)}$, where ϕ is volume fraction of particle filling, K_p^* and K_m are the thermal conductivity of the solid particle and matrix, respectively
parallel model	$\frac{K_{eff}}{K_m} = 1 + \phi(K_p^*/K_m - 1)$
Maxwell model[33]	$\frac{K_{eff}}{K_m} = \frac{(1+2\phi)K_p^*/K_m + 2(1-\phi)}{(1-\phi)K_p^*/K_m + (\phi+2)}$
inverse Maxwell model	$\frac{K_{eff}}{K_m} = \frac{2\phi K_p^*/K_m + (3-2\phi)}{(3-\phi)K_p^*/K_m + \phi}\frac{K_p^*}{K_m}$
Chiew and Glandt model[61]	$\frac{K_{eff}}{K_m} = \frac{1 + 2\beta\phi + (K_2 - 3\beta^2)\phi^2}{1 - \beta\phi}$, where $\beta = \frac{K_p^* - K_m}{K_p^* + 2K_m}$, K_2 is a function of ϕ
	the formula with fitting parameters suggested in ref 61 is $\frac{K_{eff}}{K_m} = \frac{1 + 2\beta\phi + (2\beta^3 - 0.1\beta)\phi^2 + 0.05\exp(4.5\beta)\phi^3}{1 - \beta\phi}$
Benveniste model[36]	$\frac{K_{eff}}{K_m} = \frac{2\alpha(1-\phi) + [(1+2\phi) + K_p^*/K_m(2-2\phi)]}{\alpha(2+\phi) + [(1-\phi) + K_p^*/K_m(2+2\phi)]}$
	for perfect interface, $\alpha \to 0$ $\frac{K_{eff}}{K_m} = \frac{(1+2\phi) + K_p^*/K_m(2-2\phi)}{(1-\phi) + K_p^*/K_m(2+2\phi)}$
Lewis–Nielsen model[39]	$K_{eff} = \frac{1 + AB\phi}{1 - B\psi\phi}$ A is shape factor, for sphere $A = 1.5$
	$B = \frac{K_p^*/K_m - 1}{K_p^*/K_m + A}$, $\psi = 1 + \frac{1 - \phi_m}{\phi_m^2}\phi$ ϕ_m is the maximum filler volume fraction

and FCC (Figure 3a–c), and mark the spheres at equivalent locations in the super-RVE with the same number (and color). The spheres are sequentially numbered according to their distances to the corner. Spheres with the same number must be removed simultaneously to retain cubic symmetry, and the connectivity of the spheres is checked to make sure that the resultant RVE is self-supported. Two super-RVEs created this way are shown in Figure 3d,e. The resultant packing fraction is calculated by $\varphi = F\varphi_{org}$, where F is the fraction of remained spheres and φ_{org} is the packing fraction of the original RVE. Following this procedure, 4, 6, and 13 different packing patterns are generated on the basis of the SC, BCC, and FCC super-RVEs, respectively (details are provided in the Supporting Information). Overall, 23 numerical foams with different packing patterns (packing fraction φ = 0.25–0.71) are generated in the simulation (Figures S3–S5).

Having constructed the geometric models of the HSFs, FEM simulation of ETC is based on the super-RVEs with periodic boundary conditions applied. A steady heat transfer problem without heat source can be simplified as

$$\nabla^2 T = 0 \tag{5}$$

$$\text{with } \vec{q} = -\mathbf{k}\vec{\nabla}T$$

where T is the local temperature, $\vec{q}$ is the heat flux vector, $\vec{\nabla}T$ is the temperature gradient vector, and $\mathbf{k}$ is the second rank thermal conductivity tensor. For cubic symmetric materials, $\mathbf{k}$ degrades into a constant, and the material has isotropic thermal behavior. The thermal periodic condition is realized by applying a temperature gradient along the [100] direction, while all the other surfaces are adiabatic equivalently (Figure 3f). The temperature and heat flux distributions are then solved with the commercial finite element package Abaqus (standard solver, element type DC3D4 and DC3D8), and the ETC is evaluated with Fourier's law

$$K_{eff} = \frac{\iint_S \vec{q}\, ds}{(T_1 - T_2)l} \tag{6}$$

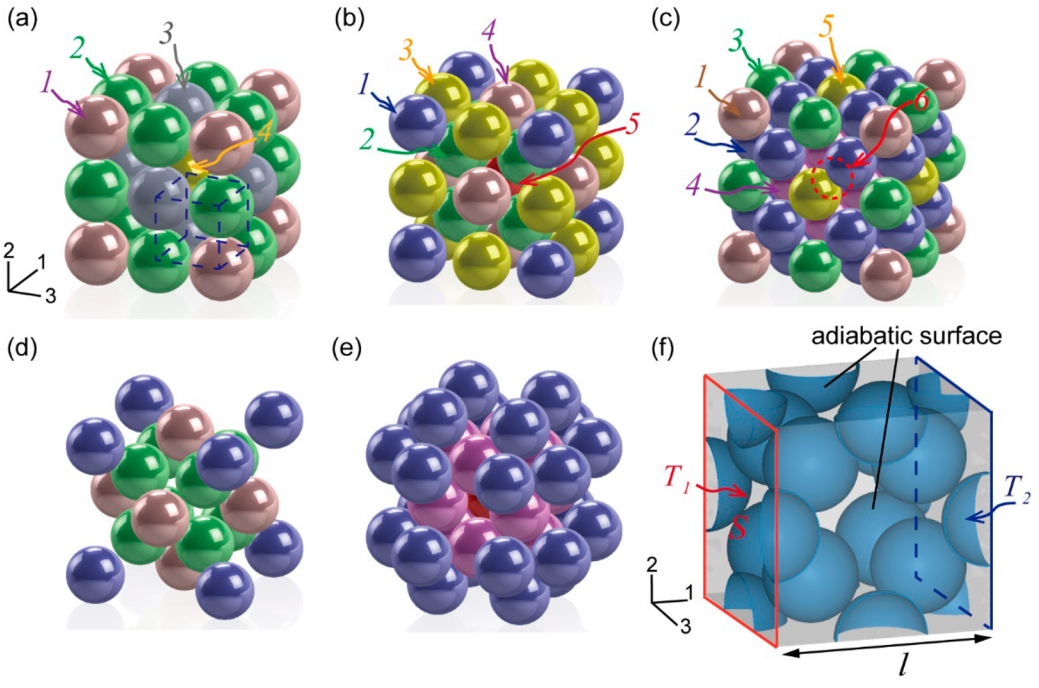

Figure 3. FEM modeling of HSFs with (a) SC (simple-cubic), (b) BCC (body-centered-cubic), (c) FCC (face-centered-cubic) packing arrangements. 2 × 2 × 2 primitive cells (the primitive cell of SC is highlighted with the dashed cube) are adopted to create a super-RVE (representative volume elements). The spheres with equivalent locations in the super-RVEs are marked with the same color, and numbered by their distance to the corner. (d) BCC based super-RVE with no. 3 (yellow) and no. 5 (red) spheres removed, leaving 3/4 of the spheres. (e) FCC based super-RVE with number 1 (brown), 3 (green), and 5 (yellow) removed, with 25/32 of the spheres retained. (f) ETC simulation based on a super-RVE. $T_1 - T_2$ is the applied temperature difference along the [100] direction, while the other surfaces are set as adiabatic. S is the area of each surface, and l is the length of the RVE.

DOI: 10.1021/acsaem.7b00264
ACS Appl. Energy Mater. 2018, 1, 1146–1157

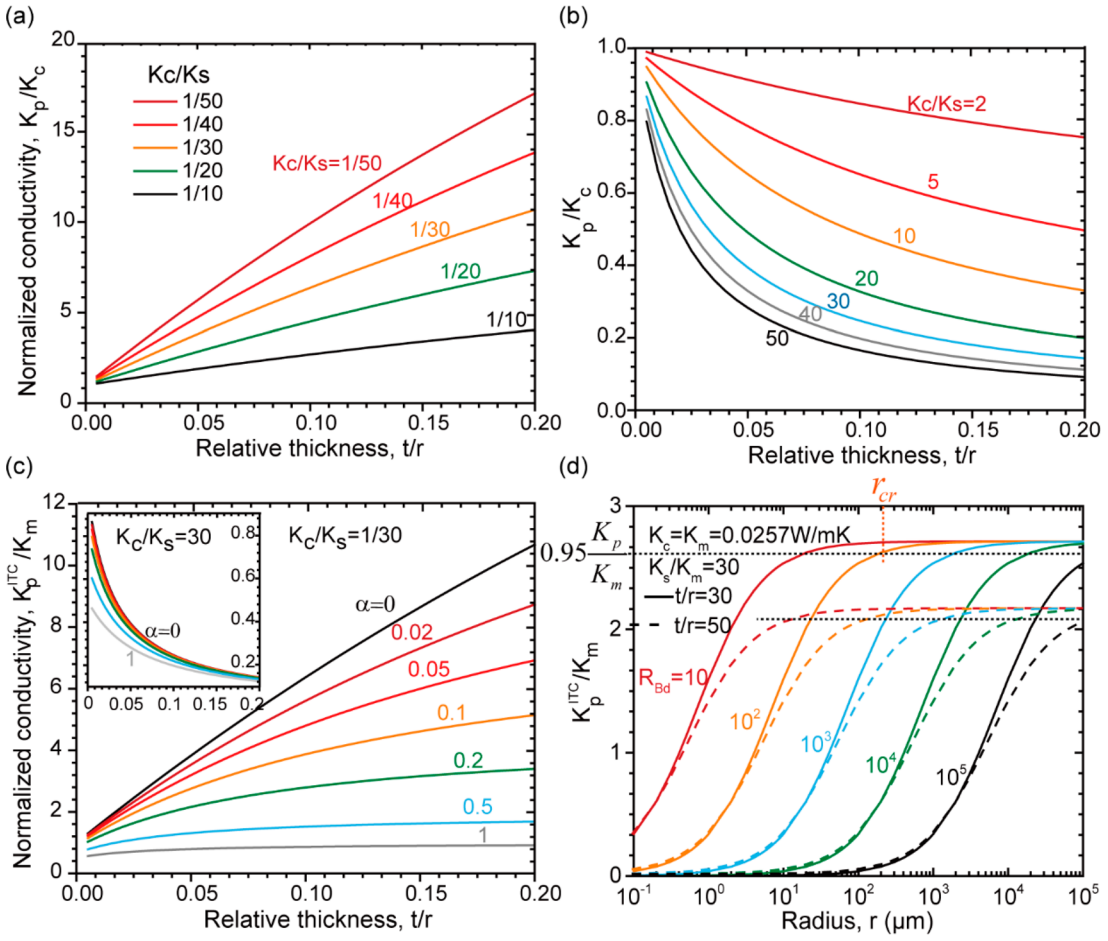

Figure 4. Hollow sphere−solid particle equivalence. Normalized conductivity of the equivalent particle plotted against relative thickness for (a) good conductive shell $K_c/K_s < 1$ and (b) poor conductive shell $K_c/K_s > 1$ without considering ITR. (c) Effect of ITR for hollow spheres with $K_c/K_s = 1/30$ and $K_c/K_s = 30$ (inset). (d) Size effect contributed by ITR at relative thickness $t/r = 1/30$ (—) and $t/r = 1/50$ (---). Also shown is the critical cell size r_{cr} for $t/r = 1/30$ and $R_{Bd} = 10^2$, which is estimated by letting $K_p^{ITC} = 0.95K_p$.

where heat flux $\vec{q}$ is integrated over the surface S, and l is the length of the unit cell. Moreover, the binder between spheres is defined by binder radius (r_b) and binder length (d_b) (Figure S2). Unless otherwise specified, the shell material used in the simulations is specified as glass (0.8 W/m K); the matrix and core material are specified as air (0.0257 W/m K), and the binder sizes are $r_b = 0.15r$, and $d_b = 0.03r$.

3. RESULTS AND DISCUSSION

3.1. Hollow Sphere−Solid Particle Equivalence. We first discuss the equivalence between a hollow sphere and a solid particle without including the ITR. Using eq 1, the conductivity of the equivalent particle (normalized by the conductivity of the core K_c) is plotted as a function of relative shell thickness t/r. Two different scenarios with $K_c < K_s$ (HSF) and $K_c > K_s$ (solid particles with poor conductive coating) are plotted in Figure 4a,b, respectively. Results show that, in both cases, the conductivity of the equivalent particle strongly depends on the shell thickness (independent of K_m), indicating that the shell thickness can be designed to tune the effective conductivity. The effect of varying ITR is then discussed with eq 4, assuming $K_c/K_s = 1/30$ (Figure 4c) and $K_c/K_s = 30$ (Figure 4c, inset). As expected, a greater α (i.e., higher ITR) leads to lower normalized conductivity K_p^{ITC}/K_m. Interestingly, K_p^{ITC} is much more sensitive to the ITR for shells with good conductivity than shells with poor conductivity. For example, when $K_c/K_s = 1/30$ and $t/r = 1/10$, the normalized conductivity reduces by 90% as α increases from 0 to 1, while the amount of reduction is about 10% for a poor conductivity shell $K_c/K_s = 30$ (Figure 4c). Note this difference is more significant for thick shells than for thin shells (see Figure S1). Moreover, this observation is consistent with the limit analysis provided in Section 2.2, which suggests that ITR is ignorable for extremely poor conductivity shells. It is also worth noting that HSFs typically have good conductivity shells; thereby, ITR should be handled carefully.

Furthermore, the size effect of ITR is highlighted when the sphere radius approaches the nanometer scale. For a specified matrix and interface, K_m and R_{Bd} are constants, so $\alpha = R_{Bd}K_m/r$ only depends on radius r, which is a source of the size effect. This dependency of K_p^{ITC} on sphere radius r is plotted in Figure 4d, with material parameters set as $K_c = K_m = 0.0257$ W/m K (air), and $K_s = 30K_m$ (glass). We find that the relative conductivity decreases rapidly with decrease of the sphere radius below a critical radius r_{cr}. One estimation of the critical size is obtained by letting $K_p^{ITC}/K_p = 0.95$, which gives $r_{cr} \approx 20R_{Bd}K_p$. The physical meaning of this ITR induced size effect is that ITR depends on the specific surface area of the interface; for spheres, the specific surface area is proportional to $1/r$, thereby, the smaller sphere size, the larger specific interfacial surface, and thus the poorer ETC. By contrast, for HSFs with r

DOI: 10.1021/acsaem.7b00264
ACS Appl. Energy Mater. 2018, 1, 1146−1157

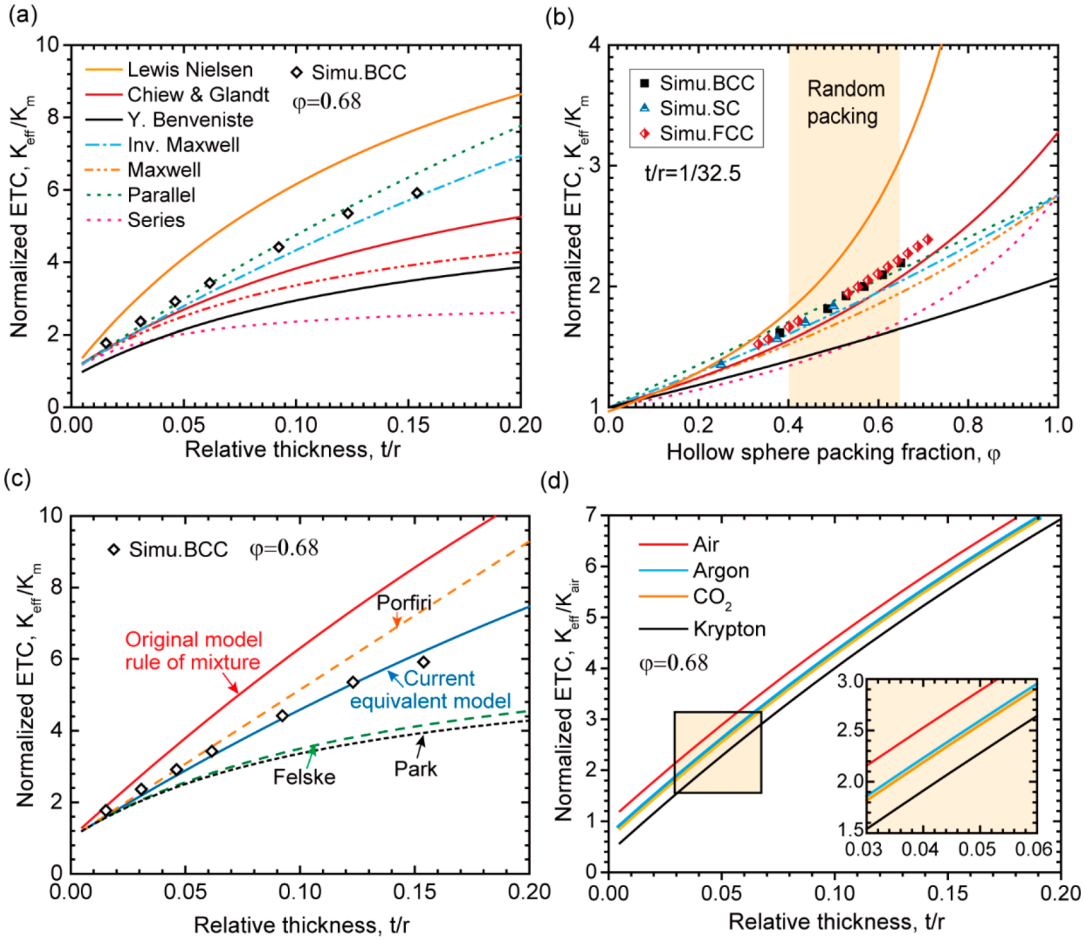

Figure 5. Verification of the theoretical predictions with FEM simulations. ETC as a function of relative thickness (fixed $\varphi = 0.68$) for parts a, c, and d, and packing fraction (fixed $t/r = 1/32.5$) for part b. The material properties are $K_s/K_m = 31$ and $K_c = K_m$ in parts a–c. The theoretical predictions are obtained by combining the equivalence relation with the models listed in Table 1. (b) The numerical results correspond to 23 numerical foams ($\varphi = 0.25$–0.71) generated on the basis of the SC, BCC, and FCC super-RVEs, which sit almost perfectly on a line indicating packing pattern independence. The shaded area shows the packing fraction range of randomly packed monosized HSFs. (c) Comparison between the original model ("rule of mixture"), syntactic foam models (Felske model, Profiri model, and Park model), and the current equivalence model (the equivalence relation combined with the parallel model). (d) Effect of low conductivity filling gases.

$> r_{cr}$, the conductivity is dominated by the hollow sphere structure instead of the ITR.

3.2. ETC Prediction of HSFs. Having found the equivalence between a hollow sphere and an equivalent particle, we then calculate the ETC of HSFs by substituting eq 4 into the models listed in Table 1. Note that the ITR is not included ($\alpha = 0$) in comparison with numerical simulations. Figure 5a,b plots the ETC as functions of relative thickness and packing fractions using the models in Table 1. Results show that the equivalence relation combined with the parallel model and inverse Maxwell models agrees well with FEM simulations, especially at small t/r; while at larger t/r, the theoretical results slightly deviate from the simulation results. This discrepancy originates in the equivalence relation, where the effective medium theory assumes small perturbations, while for a large t/r, this assumption is not accurate. Also note that although the effective medium theory alone cannot accurately predict the ETC of HSFs with percolation, when combined with the parallel model/inverse Maxwell model, the prediction is quite acceptable.

Furthermore, the ETCs of the foams with the SC, BCC, and FCC super-RVE are simulated and plotted in Figure 5b. Interestingly, regardless of the various sphere packing patterns (see Figures S3–S5), all the numerical simulation points sit almost perfectly on a curve, suggesting that the ETC of HSFs is nearly independent of packing pattern, and the packing fraction φ is the major controlling parameter. This finding is consistent with a previous report.[49] The observed packing pattern independence also suggests that the proposed theoretical model should be applicable to randomly aggregated HSFs. In addition, the packing fraction of randomly packed monosized foams satisfies $0.4 < \varphi < 0.64$,[62,63] in which range the theoretical models are quite accurate.

Next, we compare the proposed model to the broadly adopted "rule of mixture",[64–66] syntactic foam models,[50–53] and FEM simulations. The "rule of mixture" model calculates ETC by directly adding the conductivity contribution of the solid and the matrix $K_{eff} = \hat{\varphi}K_{solid} + (1-\hat{\varphi})K_{gas}$, where $\hat{\varphi}$ is the volume fraction of the solid phase.[11] Three syntactic foam models, Felske model,[50] Profiri model,[52] and Park model,[53] are chosen for comparison, where two-phase material formulas are used (see Table S1 in Supporting Information). The results in Figure 5c show that the proposed equivalent model (the equivalence relation combined with a parallel model) provides better accuracy than both the original "rule of mixture", and the syntactic foam models at $\varphi = 0.68$. The predictions from

DOI: 10.1021/acsaem.7b00264
ACS Appl. Energy Mater. 2018, 1, 1146–1157

syntactic foam models are poor because they are built for relative low particle filling fractions (syntactic foams typically have $\varphi < 0.5$),[54] and cannot accurately represent the connectivity of HSFs after percolation. Also note that the Park model can be treated as a special case of the proposed equivalent model which is the equivalence relation combined with the Maxwell model.

In addition, a low thermal conductivity gas is often used as a filling gas in the capsules of HSF to reduce the ETC in some applications.[11] For such scenarios, a three-phase materials problem ($K_c \neq K_s \neq K_s$) should be considered. To demonstrate the effect of low conductivity filling gases, we select argon (κ = 17.9 mW/m K), krypton (κ = 9.5 mW/m K), and CO_2 (κ = 6.8 mW/m K) as filling gases, and glass as the shell material (κ = 0.8 W/m K). The theoretical predictions are calculated with the equivalence relation combined with a parallel model. Figure 5d shows that the amount of reduction achieved by using a low conductivity gas is relatively constant over a wide range of relative thickness. Therefore, this reduction accounts for a substantial portion of the total ETC only at small t/r. As a result, filling low thermal conductivity gas offers an effective method for improving the thermal resistance in thin shell HSFs but not for thick shell foams.

3.3. Effect of the Shell Porosity. HSFs with microporous or mesoporous shell (see Figure 6) have received tremendous research interest in multifunctional applications like adsorption and storage, catalysis, and biomedicine.[20,22,32] The subtle combination of the hollow architecture with the porous shell structure brings special characteristics like extraordinarily large specific surface, efficient transfer of reactants and products, and a much smaller diffusion length.[22,67] Aside from the multifunction, shell porosity may also significantly modify the ETC of HSFs, which should be considered properly. Here, we inspect the effect of shell porosity from two aspects: (1) partially removed shell material and (2) Knudsen effect inside the microporous shell.

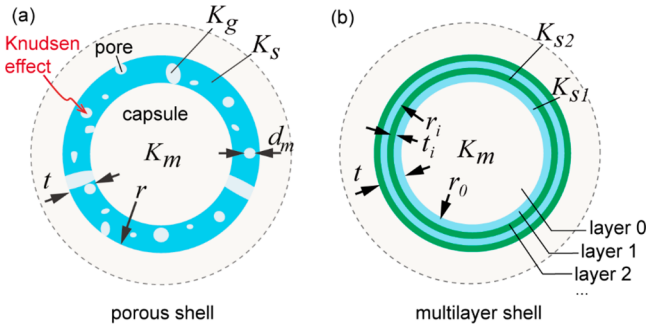

Figure 6. Schematic of hollow spheres with a porous shell and a multilayer shell. (a) Porous shell sphere with shell porosity P, and mean pore size d_m. Gas conductivity in the pores K_g is controlled by the Knudsen effect, while no Knudsen effect takes place inside the hollow sphere capsule (suppose $r > 1$ μm). (b) Multilayer shell with two alternating shell materials, layers are numbered from inside as layer 0, 1, 2, ..., N, and t_i, r_i are the thickness and radius of the ith layer.

To investigate the effect of removing shell material (see Figure 6a), we first treat the porous shell as a homogeneous solid material (with K_{eff}^{shell}) using the Maxwell model[33]

$$\frac{K_{eff}^{shell}}{K_s} = \frac{(1+2P)K_g/K_s + 2(1-P)}{(1-P)K_g/K_s + (P+2)} \quad (7)$$

where P is the shell porosity, K_g is the gas conductivity in the pore, and K_s is the conductivity of the constituent shell material. We then calculated the ETC of HSF with porous shell by combining eqs 1 and 7 with the proposed equivalent model. Figure 7a shows the resultant ETC plotted against shell porosity with four different shell materials, Al (κ = 200 W/m K), Al_2O_3 (κ = 20 W/m K), glass (κ = 0.8 W/m K), and silica (κ = 1.4 W/m K). For the glass HSF, 50% shell porosity reduces the total ETC by 31%, while for the Al foam the reduction is up to 50%. This strong dependency on shell porosity makes sense because shell material is the main contributor to the total ETC; thus, removing shell material reduces the ETC considerably.

Next, we investigate the Knudsen effect on the shell porosity, a partial suppression of gaseous thermal conductivity induced by small size, which is known to have a significant influence on nanoscale foams, e.g., aerogel and nanosized silica foams. Since the Knudsen effect inside the hollow sphere capsule has been well-studied,[64−66] here we only consider this effect inside the pores of the shell. To do so, we assume the hollow sphere radius $r > 1$ μm, which guarantees that the Knudsen effect inside the capsule of hollow sphere is ignorable. The frequently used formula for estimating the gaseous thermal conductivity with Knudsen effect is[64,68]

$$K_g = \frac{K_g^0}{1 + 2\varsigma Kn} \quad (8)$$

where ζ is a parameter that considers the energy transfer between gas molecules and the limiting structure (for air $\zeta \approx 2$) and K_g^0 is the thermal conductivity of a free gas at atmospheric pressure. Kn is the Knudsen number defined as $Kn = l_m/d_m$; d_m is the mean pore size, and l_m is the mean free path of gas molecules in free space, evaluated by[56]

$$l_m = \frac{k_B T}{\sqrt{2}\pi d_g^2 p} \quad (9)$$

where k_B is the Boltzmann constant ($k_B = 1.38 \times 10^{-23}$ J K^{-1}), T and p are the gas temperature and pressure, and d_g is the diameter of the gas molecule ($d_g = 3.798 \times 10^{-10}$ m for nitrogen).

The evolution of K_g with respect to the pore size d_m is shown in Figure 7b, inset, which decreases rapidly when pore size decreases from 1 μm to 10 nm. The effect of the Knudsen effect on the ETC of the microporous HSF ($K_{eff}^{d_m}$, pore size d_m) is then calculated by substituting eq 8 in eq 7, and following the equivalent model. Note that $K_{eff}^{d_m}$ is normalized by HSF with the same shell porosity but a large pore size $K_{eff}^{d_m=\infty}$ to highlight the Knudsen effect. Quite unexpectedly, the reduction of ETC induced by Knudsen effect inside the porous shell is very small, as presented in Figure 7b ($K_{eff}^{d_m}/K_{eff}^{d_m=\infty}$ decreases less than 5% even for 80% shell porosity). The reason is that the pores in the shell have both a small total volume fraction and a small K_g^0/K_s.

3.4. Effect of the Multilayer Shell. Another interesting design of the hollow spheres is the multilayer shell structure shown in Figure 6b. Multilayer shell hollow spheres are often used in drug release[69] and acoustic cloaking.[70] Recently, multilayer HSFs are adopted in designing supercapacitors[25,26] and electrochemical energy storage devices,[30] since the hollow structure can provide a larger accessible surface area that facilitates charge and ion transport. Moreover, spheres with multilayer shells are proven to be a new type of thermal metamaterial, exhibiting remarkable thermal shielding abil-

DOI: 10.1021/acsaem.7b00264
ACS Appl. Energy Mater. 2018, 1, 1146−1157

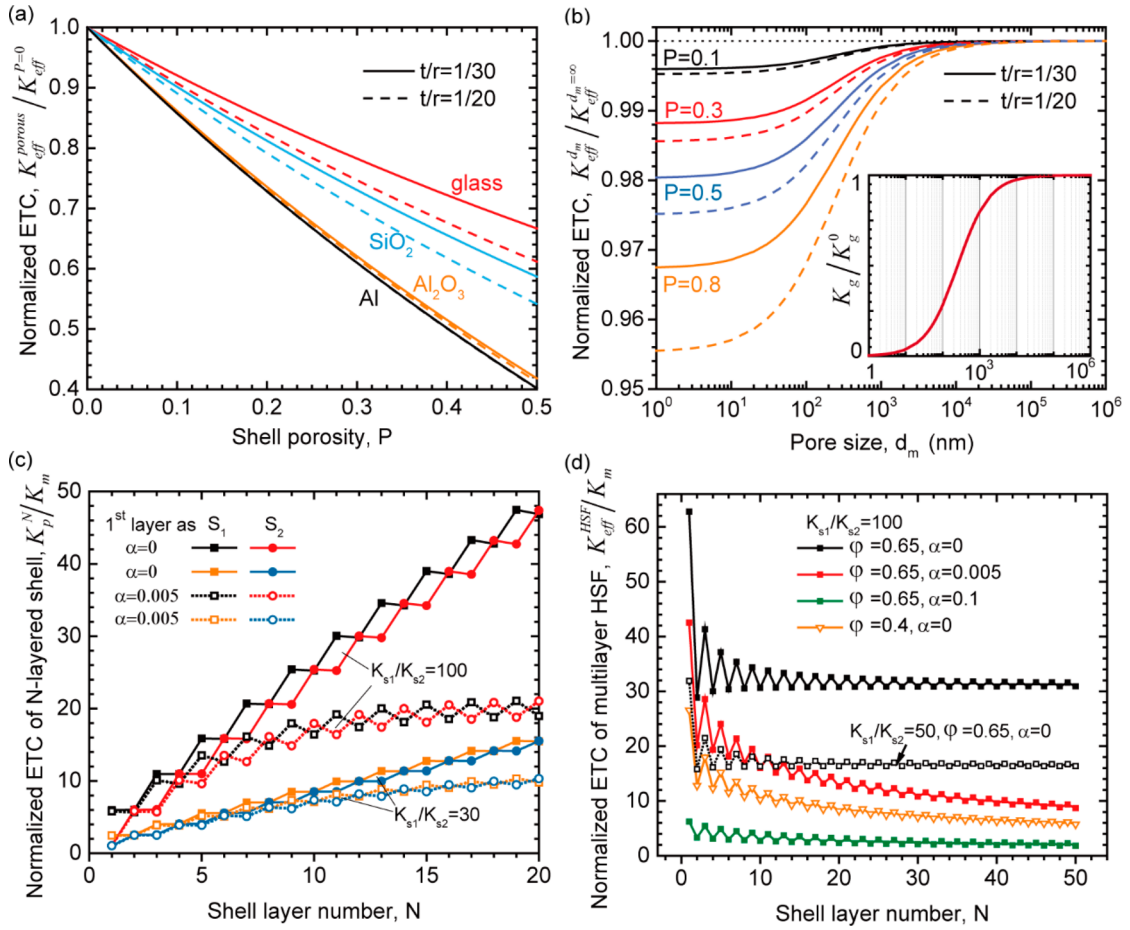

Figure 7. Effect of shell porosity and multilayer shell. (a) Normalized ETC plot as a function of shell porosity, $K_{eff}^{porous}/K_{eff}^{P=0}$ is the ETC of porous shell foam normalized by ETC of foam with no shell porosity. Four typical shell materials are plotted as Al, $A1_2O_3$, glass, and silica; the matrix material is air. (b) Knudsen effect with respect to the pore size. $K_{eff}^{d_m}/K_{eff}^{d_m=\infty}$ is the ETC of porous shell with mean pore size d_m normalized by porous shell with a large pore size (no Knudsen effect). (c) ETC of the equivalent particle with N-layer shell K_p^N normalized by ETC of the matrix versus layer number N. Two shell conductivity ratios K_{S1}/K_{S2} = 30, 100; two shell material sequences (1st layer material is S1 or S2) and two ITRs (α = 0, 0.005) are plotted for comparison. (d) Normalized ETC of the multilayered shell HSF K_{eff}^{HSF}/K_m versus layer number N, with fixed total shell thickness $t = r/20$. The influences of packing fraction φ, ITR, and K_{S1}/K_{S2} are presented.

ity.[71,72] In such applications, the thermal or electrical conductivity are matters of great concern. With the knowledge that the thermal conduction problem and electrical conduction are governed by similar equations and are thus equivalent, our discussion here focuses on the ETC (i.e., thermal conduction problem) of the multilayer HSFs. To estimate the ETC of multilayer shell materials, a layer by layer calculation is applied. For a multilayer shell, the layers are numbered as 0, 1, 2, ..., N from the innermost layer, with the core denoted as layer 0 (Figure 6b). We assume two shell materials are deposited alternatively, denoted as material 1 (S1) and material 2 (S2). Noting eq 4 as a function f, the ETC of an equivalent particle with 0 to i + 1 layer shells can be written in a recursive relationship as

$$\frac{K_p^{i+1}}{K_m} = f\left(\frac{K_p^i}{K_{Sj}}, \frac{K_m}{K_{Sj}}, \alpha_i, \frac{t_i}{r_i}\right) \qquad 0 < i < N \tag{10}$$

$$\text{with } \sum_{i=1}^{N} t_i = t \text{ and } \begin{cases} j = 1, \text{ odd } i \\ j = 2, \text{ even } i \end{cases}$$

where t_i, r_i, and α_i are the thickness, outer radius, and ITR for the ith layer, respectively, K_{S1} and K_{S2} are the shell conductivity for material S1 and material S2, respectively, and t is the total shell thickness. For simplicity, it is supposed that each layer has the same thickness $t_i = t/N$; thus, $r_i = r_0 + it/N$.

The equivalent particle conductivity K_p^N (with N layer shell) is then solved with eq 10. The effect of varying layer sequence, the ITR, and shell conductivity ratio are plotted against the total layer number N (with fixed $t_i = r/400$ and K_{S2}/K_m = 10) in Figure 7c. Note the two possible shell material sequences are layer 1 with material S1 (Figure 6b), or layer 1 with material S2. Interestingly, when N increases, K_p^N varies along a zigzag polyline and approaches a limit value. In addition, since there are N + 1 interfaces, the conductivity is very sensitive to the ITR; even a small α (0.005) has a noteworthy influence on K_p^N.

With K_p^N determined, we further explore the ETC of foams packed by spheres with multilayer shells. Without loss of generality, we study the effect of increasing layer number with the total shell thickness fixed ($t = r/20$), $t_i = t/N$, K_{S2}/K_m = 10, and set the material of the first layer as S1. The influences of packing fraction, ITR, and shell material are summarized in Figure 7d. Results show that lower packing fraction, lower shell conductivity, and higher ITR lead to lower thermal conductivity. The ETC is more sensitive to layer number at small N, while for large N, ETC approaches a limit controlled

DOI: 10.1021/acsaem.7b00264
ACS Appl. Energy Mater. 2018, 1, 1146−1157

by packing fraction and ITR. Interestingly, the ETC of an odd layer number is more sensitive to N than an even number. Therefore, proper total layer number and material sequence can be selected to tune the ETC (and electrical conductivity) of multilayer shell HSF.

3.5. Effect of Sphere Sizes. So far, our discussions are based on monosized HSFs, but the constituent hollow spheres might have a size distribution, as depicted in Figure 1b. In our theoretical model, the two controlling parameters are shell relative thickness t/r and packing fraction φ, which cannot deal with size distribution directly. However, the sphere size distribution will have effect on φ, which in turn affects the ETC. To find out whether the model will have a reasonable prediction of HSF with size distribution, here we numerically constructed HSF with two sphere sizes in the super-RVE. As shown in Figure 8a, the size of no. 2 spheres (occupying 50% of the total spheres) is either decreased by 20%, or enlarged by 20%, and then part of the spheres is removed in a manner similar to the procedure described in Section 2.4. Note that the relative thickness of all spheres is kept constant when the sphere radius is scaled. Figure 8b shows that the Chiew and Glandt model, parallel model, and inverse Maxwell model give acceptable predictions. Interestingly, for spheres with size distribution, the Chiew and Glandt model best depicts the trend of the numerical results (but not for monosized foams), which suggests the versatility of the proposed model. More importantly, the numerical simulation points stay within a relatively narrow band in Figure 8b, indicating that the sphere size distribution also has a relatively insignificant influence on the ETC.

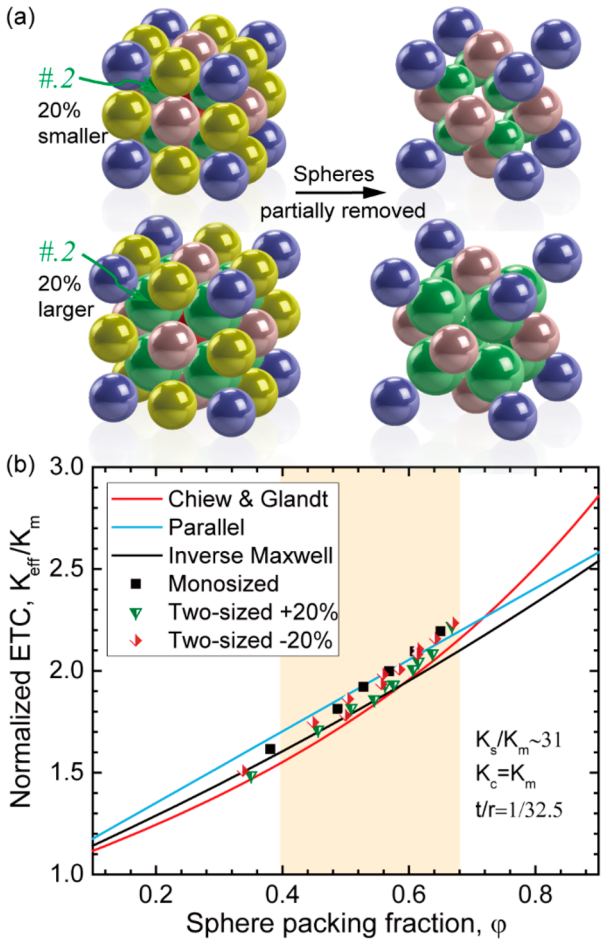

Figure 8. Effect of sphere sizes. (a) Upper part shows RVE with the no. 2 sphere (green) size decreased by 20%, and the bottom part shows the no. 2 sphere size enlarged by 20%. (b) Monosized BCC packing foams compared with BCC packing with two sphere sizes, with different packing fractions achieved by partially removal of the spheres.

3.6. Effect of the Binder Shape. For foams generated by sintering or binding the spheres together, a connecting binder between spheres is generally found (Figure 1b).[9] A typical binder can be defined by the binder radius r_b and binder length d_b (minimum distance between two adjacent spheres) as shown in Figure 9a, inset. The effects of binder radius and length on ETC are studied numerically by constructing foams with different binder sizes. Note that the theoretical models cannot directly predict the effect of varying binder radius, and the effect of binder length change is also included in the packing fraction. Two binder radii $r_b = 0.15r$ and $0.13r$ are plotted as a function of relative thickness with binder thickness fixed at $d_b/r = 1/32.5$. As expected, a large r_b contributes to a larger ETC (Figure 9a), but the influence of binder radius is found to be insignificant. By contrast, the effect of varying binder length d_b ($t/r = 1/32.5$) is found to have a more significant influence on the ETC (see Figure 9b), since it has a large influence on the packing fraction of the spheres. The observation that ETC is more sensitive to binder length (strongly affects φ) than binder radius (does not affect φ) confirmed that φ is a key parameter controlling the ETC.

3.7. Design Space. In most multifunctional HSF designs, acceptable mechanical properties are often required, since the device should have certain stiffness and strength to support loads. Here the materials property chart[75] is used to visualize the correlations between thermal and mechanical properties of HSFs. Figure 10 plots the ETC against Young's modulus for HSF with varying materials, relative shell thicknesses, and packing patterns. Three shell materials (Al, $A1_2O_3$, and glass) are plotted with t/r varying from 0.01 to 0.2. The theoretical ETC predictions are calculated with the proposed equivalent model, and $0.4 < \varphi < 0.64$ is used to estimate the ETC of randomly packed foams,[63] while the SC, BCC, and FCC packed foams are evaluated with φ of 0.52, 0.68, and 0.74, respectively. The Young's modulus is calculated with the fitted equations proposed in papers.[73,74] Numerical results of ETC and Young's modulus of HSF with BCC packing are also obtained with FEM simulation based on periodic boundary conditions[76,77] with $r_b = 0.3r$, $d_b/r = 1/32.5$. The results show a very wide design space of HSFs enabled by varying materials, packing patterns, packing fractions, and relative thicknesses. Such a wide design space, together with the further design of shell porosity and multilayer shell, makes hollow sphere foam materials very versatile and promising as engineering materials. In addition, our recent study[44] shows that introducing hierarchy could reduce ETC while improve stiffness.

4. CONCLUSION

In this work, we have presented a micromechanical model that accurately predicts the effective thermal conductivity of hollow sphere foam materials. This model takes advantage of the models previously developed for solid particle filled composites; thus, it is easy to use and versatile. As a demonstration, the proposed model is applied to study the effect of varying sphere packing fractions, filling gases, porous shells, and multilayer shells. The results are further verified by FEM

DOI: 10.1021/acsaem.7b00264
ACS Appl. Energy Mater. 2018, 1, 1146−1157

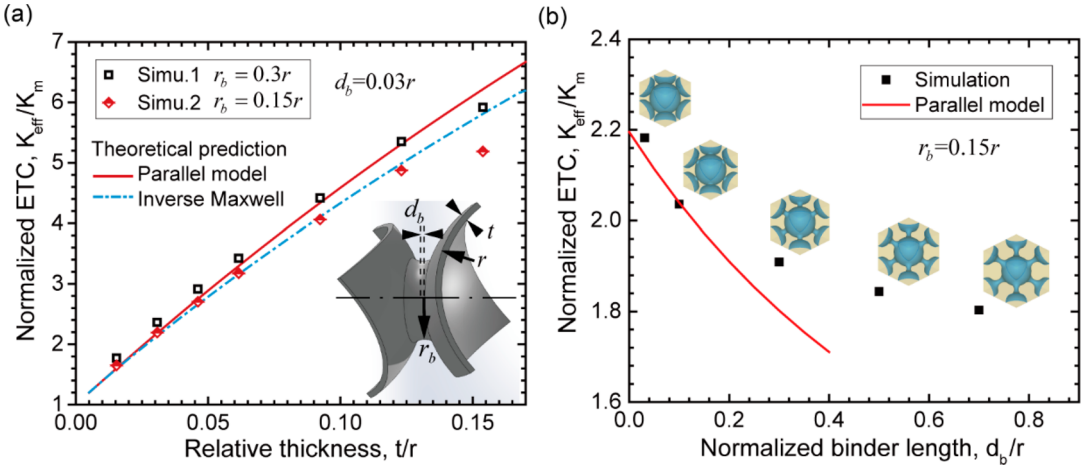

Figure 9. Effect of the binder shape. The red line/dotted line shows the proposed equivalent model combined with a parallel model/inverse Maxwell model, and the points are the results of numerical simulations. (a) ETC plotted as a function of t/r, with binder radius $r_b = 0.15r$ and $0.3r$ (theoretical result is calculated with $\varphi = 0.68$). The binder geometry definition is shown in the inset. (b) Effect of changing binder length on the ETC. The theoretical prediction is obtained by varying φ based on the variation of d_b.

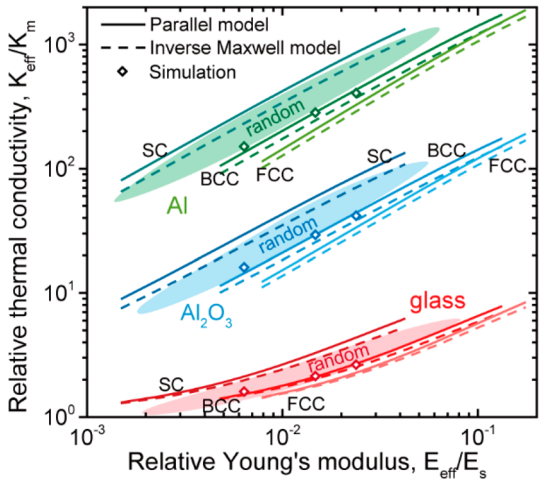

Figure 10. Materials property chart for monosized HSF; ETCs are plotted against the relative Young's modulus. Lines show theoretical prediction of SC, BCC, and FCC packing foams. Relative ETC is calculated by the proposed ETC model combined with the parallel model (—) and the inverse Maxwell model (---). Relative Young's modulus is calculated with equations proposed in refs 73 and 74. The points show the FEM simulation results, and the shadows indicate the regions of randomly packed foams.

simulations, showing that the model provides accurate ETC prediction of HSFs with different packing patterns, binder shapes, and sphere size. More importantly, this work provides insights into hollow sphere foam design through parametric studies. For instance, aside from the well-known key parameters (sphere relative thickness and sphere packing fraction), we highlight that ITR, nanosize, shell porosity, binder length, and multilayer sequence are other important features that can be used to design low (or tunable) ETC and multifunctional HSFs.

Furthermore, two sources of size effect have been evaluated to extend the model to nanosized HSFs, namely, the Knudsen effect and the interfacial thermal resistance effect. Both effects tend to increase thermal resistance at a smaller length scale, suggesting that a "small characteristic length scale" might be important to produce HSFs with extremely low thermal conductivity. The Knudsen effect takes place in the HSF capsule at cell size smaller than 1 μm (air). By contrast, the ITR induced size effect should be considered at cell size smaller than $20R_{Bd}K_p$. Surprisingly, the Knudsen effect within the porous shell is found to be insignificant regardless of the pore size. In addition, since the governing equations are essentially the same for thermal and electrical conduction problems, a similar procedure can be adopted to predict the effective electric conductivity of HSF. The findings reported here provide a new route to estimate the ETC of HSFs, paving the way to design traditional, nanoscale, microporous, and multilayer shell HSFs with novel multifunctional applications.

■ ASSOCIATED CONTENT

Supporting Information

The Supporting Information is available free of charge on the ACS Publications website at DOI: 10.1021/acsaem.7b00264.

Derivation of the equivalent relation (eq 1); derivation of ETC of a solid particle with ITR (eq 3); list of syntactic foam ETC formulas; comparison between the ITR effect for shells with good conductivity and shells with poor conductivity; details of binder modeling; method for super-RVE generation; SC, BCC, and FCC primitive cells based super-RVEs; and mechanical simulation method (PDF)

■ AUTHOR INFORMATION

Corresponding Author

*E-mail: Lifeng.wang@stonybrook.edu.

ORCID

David Hwang: 0000-0002-9928-1484

Lifeng Wang: 0000-0002-2068-5102

Notes

The authors declare no competing financial interest.

■ ACKNOWLEDGMENTS

The authors gratefully acknowledge the support from the National Science Foundation (CMMI-1462270) and the Office of Naval Research (Dr. Yapa Rajapakse, Solid Mechanics Program).

DOI: 10.1021/acsaem.7b00264
ACS Appl. Energy Mater. 2018, 1, 1146−1157

REFERENCES

(1) Andersen, O.; Waag, U.; Schneider, L.; Stephani, G.; Kieback, B. Novel Metallic Hollow Sphere Structures. *Adv. Eng. Mater.* **2000**, *2*, 192−195.

(2) Zeng, H.; Pattofatto, S.; Zhao, H.; Girard, Y.; Fascio, V. Impact Behaviour of Hollow Sphere Agglomerates with Density Gradient. *Int. J. Mech. Sci.* **2010**, *52*, 680−688.

(3) Zhu, Y.; Liang, S.; Chen, K.; Gao, X.; Chang, P.; Tian, C.; Wang, J.; Huang, Y. Preparation and Properties of Nanoencapsulated N-Octadecane Phase Change Material with Organosilica Shell for Thermal Energy Storage. *Energy Convers. Manage.* **2015**, *105*, 908−917.

(4) Cochran, J. K. Ceramic Hollow Spheres and Their Applications. *Curr. Opin. Solid State Mater. Sci.* **1998**, *3*, 474−479.

(5) Pan, L.; Chortos, A.; Yu, G.; Wang, Y.; Isaacson, S.; Allen, R.; Shi, Y.; Dauskardt, R.; Bao, Z. An Ultra-Sensitive Resistive Pressure Sensor Based on Hollow-Sphere Microstructure Induced Elasticity in Conducting Polymer Film. *Nat. Commun.* **2014**, *5*, 3002.

(6) Li, X.-L.; Lou, T.-J.; Sun, X.-M.; Li, Y.-D. Highly Sensitive Wo3 Hollow-Sphere Gas Sensors. *Inorg. Chem.* **2004**, *43*, 5442−5449.

(7) Caruso, F.; Caruso, R. A.; Möhwald, H. Nanoengineering of Inorganic and Hybrid Hollow Spheres by Colloidal Templating. *Science* **1998**, *282*, 1111−1114.

(8) Fowler, C. E.; Khushalani, D.; Mann, S. Facile Synthesis of Hollow Silica Microspheres. *J. Mater. Chem.* **2001**, *11*, 1968−1971.

(9) Wang, Z.; Zhang, T.; Park, B. K.; Lee, W. I.; Hwang, D. J. Minimal Contact Formation between Hollow Glass Microparticles toward Low-Density and Thermally Insulating Composite Materials. *J. Mater. Sci.* **2017**, *52*, 6726−6740.

(10) Ashby, M. F.; Evans, T.; Fleck, N. A.; Hutchinson, J.; Wadley, H.; Gibson, L. *Metal Foams: A Design Guide*; Butterworth-Heinemann, 2000.

(11) Gibson, L. J.; Ashby, M. F. *Cellular Solids: Structure and Properties*; Cambridge University Press: 1999.

(12) Fowler, C. E.; Khushalani, D.; Mann, S. Interfacial Synthesis of Hollow Microspheres of Mesostructured Silica. *Chem. Commun.* **2001**, 2028−2029.

(13) Li, Y.; Yang, Y.; Shi, J.; Ruan, M. Synthesis and Characterization of Hollow Mesoporous Carbon Spheres with a Highly Ordered Bicontinuous Cubic Mesostructure. *Microporous Mesoporous Mater.* **2008**, *112*, 597−602.

(14) Kato, N.; Ishii, T.; Koumoto, S. Synthesis of Monodisperse Mesoporous Silica Hollow Microcapsules and Their Release of Loaded Materials. *Langmuir* **2010**, *26*, 14334−14344.

(15) Lin, M.-H.; Chen, H.-Y.; Gwo, S. Layer-by-Layer Assembly of Three-Dimensional Colloidal Supercrystals with Tunable Plasmonic Properties. *J. Am. Chem. Soc.* **2010**, *132*, 11259−11263.

(16) Dong, A.; Ye, X.; Chen, J.; Murray, C. B. Two-Dimensional Binary and Ternary Nanocrystal Superlattices: The Case of Monolayers and Bilayers. *Nano Lett.* **2011**, *11*, 1804−1809.

(17) Henzie, J.; Grünwald, M.; Widmer-Cooper, A.; Geissler, P. L.; Yang, P. Self-Assembly of Uniform Polyhedral Silver Nanocrystals into Densest Packings and Exotic Superlattices. *Nat. Mater.* **2012**, *11*, 131−137.

(18) Yin, J.; Retsch, M.; Thomas, E. L.; Boyce, M. C. Collective Mechanical Behavior of Multilayer Colloidal Arrays of Hollow Nanoparticles. *Langmuir* **2012**, *28*, 5580−5588.

(19) Yin, J.; Retsch, M.; Lee, J. H.; Thomas, E. L.; Boyce, M. C. Mechanics of Nanoindentation on a Monolayer of Colloidal Hollow Nanoparticles. *Langmuir* **2011**, *27*, 10492−10500.

(20) Kresge, C.; Leonowicz, M.; Roth, W.; Vartuli, J.; Beck, J. Ordered Mesoporous Molecular Sieves Synthesized by a Liquid-Crystal Template Mechanism. *Nature* **1992**, *359*, 710−712.

(21) Schacht, S.; Huo, Q.; Voigt-Martin, I.; Stucky, G.; Schüth, F. Oil-Water Interface Templating of Mesoporous Macroscale Structures. *Science* **1996**, *273*, 768−771.

(22) Li, Y.; Shi, J. Hollow-Structured Mesoporous Materials: Chemical Synthesis, Functionalization and Applications. *Adv. Mater.* **2014**, *26*, 3176−3205.

(23) Jiang, P.; Bertone, J. F.; Colvin, V. L. A Lost-Wax Approach to Monodisperse Colloids and Their Crystals. *Science* **2001**, *291*, 453−457.

(24) Sadovoy, A. V.; Lomova, M. V.; Antipina, M. N.; Braun, N. A.; Sukhorukov, G. B.; Kiryukhin, M. V. Layer-by-Layer Assembled Multilayer Shells for Encapsulation and Release of Fragrance. *ACS Appl. Mater. Interfaces* **2013**, *5*, 8948−8954.

(25) Luo, J.; Ma, Q.; Gu, H.; Zheng, Y.; Liu, X. Three-Dimensional Graphene-Polyaniline Hybrid Hollow Spheres by Layer-by-Layer Assembly for Application in Supercapacitor. *Electrochim. Acta* **2015**, *173*, 184−192.

(26) Mu, B.; Zhang, W.; Wang, A. Template Synthesis of Graphene/Polyaniline Hybrid Hollow Microspheres as Electrode Materials for High-Performance Supercapacitor. *J. Nanopart. Res.* **2014**, *16*, 2432.

(27) Dou, J.; Zeng, H. C. Targeted Synthesis of Silicomolybdic Acid (Keggin Acid) inside Mesoporous Silica Hollow Spheres for Friedel−Crafts Alkylation. *J. Am. Chem. Soc.* **2012**, *134*, 16235−16246.

(28) Wang, Y.; Wang, D.; Tan, M.; Jiang, B.; Zheng, J.; Tsubaki, N.; Wu, M. Monodispersed Hollow So3h-Functionalized Carbon/Silica as Efficient Solid Acid Catalyst for Esterification of Oleic Acid. *ACS Appl. Mater. Interfaces* **2015**, *7*, 26767−26775.

(29) Wang, Y.; Cai, J.; Wu, M.; Zhang, H.; Meng, M.; Tian, Y.; Ding, T.; Gong, J.; Jiang, Z.; Li, X. Hydrogenated Cagelike Titania Hollow Spherical Photocatalysts for Hydrogen Evolution under Simulated Solar Light Irradiation. *ACS Appl. Mater. Interfaces* **2016**, *8*, 23006−23014.

(30) Rengarajan, R.; Jiang, P.; Colvin, V.; Mittleman, D. Optical Properties of a Photonic Crystal of Hollow Spherical Shells. *Appl. Phys. Lett.* **2000**, *77*, 3517−3519.

(31) Xu, X.; Asher, S. A. Synthesis and Utilization of Monodisperse Hollow Polymeric Particles in Photonic Crystals. *J. Am. Chem. Soc.* **2004**, *126*, 7940−7945.

(32) Zhu, J.; Tang, C.; Zhuang, Z.; Shi, C.; Li, N.; Zhou, L.; Mai, L. Porous and Low-Crystalline Manganese Silicate Hollow Spheres Wired by Graphene Oxide for High-Performance Lithium and Sodium Storage. *ACS Appl. Mater. Interfaces* **2017**, *9*, 24584−24590.

(33) Maxwell, J. C. *A Treatise on Electricity and Magnetism*; Clarendon Press, 1881; Vol. *1*.

(34) Rayleigh, L. On the Influence of Obstacles Arranged in Rectangular Order Upon the Properties of a Medium. *Philos. Mag.* **1892**, *34*, 481−502.

(35) Landauer, R. The Electrical Resistance of Binary Metallic Mixtures. *J. Appl. Phys.* **1952**, *23*, 779−784.

(36) Benveniste, Y. Effective Thermal Conductivity of Composites with a Thermal Contact Resistance between the Constituents: Nondilute Case. *J. Appl. Phys.* **1987**, *61*, 2840−2843.

(37) Hasselman, D.; Johnson, L. F. Effective Thermal Conductivity of Composites with Interfacial Thermal Barrier Resistance. *J. Compos. Mater.* **1987**, *21*, 508−515.

(38) Nan, C.-W.; Birringer, R.; Clarke, D. R.; Gleiter, H. Effective Thermal Conductivity of Particulate Composites with Interfacial Thermal Resistance. *J. Appl. Phys.* **1997**, *81*, 6692−6699.

(39) Pietrak, K.; Wisniewski, T. S. A Review of Models for Effective Thermal Conductivity of Composite Materials. *J. Power Technol.* **2015**, *95*, 14.

(40) Van Antwerpen, W.; Du Toit, C.; Rousseau, P. A Review of Correlations to Model the Packing Structure and Effective Thermal Conductivity in Packed Beds of Mono-Sized Spherical Particles. *Nucl. Eng. Des.* **2010**, *240*, 1803−1818.

(41) Landauer, R.; Garland, J.; Tanner, D. Electrical Conductivity in Inhomogeneous Media. In *AIP Conference Proceedings*; AIP, 1978; pp 2−45.

(42) Ganapathy, D.; Singh, K.; Phelan, P. E.; Prasher, R. An Effective Unit Cell Approach to Compute the Thermal Conductivity of Composites with Cylindrical Particles. *J. Heat Transfer* **2005**, *127*, 553−559.

(43) Ramani, K.; Vaidyanathan, A. Finite Element Analysis of Effective Thermal Conductivity of Filled Polymeric Composites. *J. Compos. Mater.* **1995**, *29*, 1725−1740.

DOI: 10.1021/acsaem.7b00264
ACS Appl. Energy Mater. 2018, 1, 1146−1157

(44) Chen, Y.; Jia, Z.; Wang, L. Hierarchical Honeycomb Lattice Metamaterials with Improved Thermal Resistance and Mechanical Properties. *Compos. Struct.* **2016**, *152*, 395−402.
(45) Wang, M.; Wang, J.; Pan, N.; Chen, S. Mesoscopic Predictions of the Effective Thermal Conductivity for Microscale Random Porous Media. *Phys. Rev. E* **2007**, *75*, 036702.
(46) Fang, W.-Z.; Chen, L.; Gou, J.-J.; Tao, W.-Q. Predictions of Effective Thermal Conductivities for Three-Dimensional Four-Directional Braided Composites Using the Lattice Boltzmann Method. *Int. J. Heat Mass Transfer* **2016**, *92*, 120−130.
(47) Solórzano, E.; Rodríguez-Perez, M.; de Saja, J. Thermal Conductivity of Metallic Hollow Sphere Structures: An Experimental, Analytical and Comparative Study. *Mater. Lett.* **2009**, *63*, 1128−1130.
(48) Liang, J.; Li, F. Measurement of Thermal Conductivity of Hollow Glass-Bead-Filled Polypropylene Composites. *Polym. Test.* **2006**, *25*, 527−531.
(49) Thiele, A. M.; Kumar, A.; Sant, G.; Pilon, L. Effective Thermal Conductivity of Three-Component Composites Containing Spherical Capsules. *Int. J. Heat Mass Transfer* **2014**, *73*, 177−185.
(50) Felske, J. Effective Thermal Conductivity of Composite Spheres in a Continuous Medium with Contact Resistance. *Int. J. Heat Mass Transfer* **2004**, *47*, 3453−3461.
(51) Pal, R. Thermal Conductivity of Three-Component Composites of Core-Shell Particles. *Mater. Sci. Eng., A* **2008**, *498*, 135−141.
(52) Porfiri, M.; Nguyen, N.; Gupta, N. Thermal Conductivity of Multiphase Particulate Composite Materials. *J. Mater. Sci.* **2009**, *44*, 1540−1550.
(53) Park, Y. K.; Kim, J.-G.; Lee, J.-K. Prediction of Thermal Conductivity of Composites with Spherical Microballoons. *Mater. Trans.* **2008**, *49*, 2781−2785.
(54) Gupta, N.; Pinisetty, D. A Review of Thermal Conductivity of Polymer Matrix Syntactic Foams—Effect of Hollow Particle Wall Thickness and Volume Fraction. *JOM* **2013**, *65*, 234−245.
(55) Augustin, C. *Multifunctional Metallic Hollow Sphere Structures: Manufacturing, Properties and Application*; Springer-Verlag: Berlin, 2009.
(56) Nan, C.-W. Physics of Inhomogeneous Inorganic Materials. *Prog. Mater. Sci.* **1993**, *37*, 1−116.
(57) Swartz, E. T.; Pohl, R. O. Thermal Boundary Resistance. *Rev. Mod. Phys.* **1989**, *61*, 605.
(58) Pollack, G. L. Kapitza Resistance. *Rev. Mod. Phys.* **1969**, *41*, 48.
(59) Mikic, B. B. Thermal Contact Resistance. Ph.D dissertation. Massachusetts Institute of Technology, 1967.
(60) Maldovan, M. Narrow Low-Frequency Spectrum and Heat Management by Thermocrystals. *Phys. Rev. Lett.* **2013**, *110*, 025902.
(61) Chiew, Y.; Glandt, E. The Effect of Structure on the Conductivity of a Dispersion. *J. Colloid Interface Sci.* **1983**, *94*, 90−104.
(62) Song, C.; Wang, P.; Makse, H. A. A Phase Diagram for Jammed Matter. *Nature* **2008**, *453*, 629−632.
(63) Clusel, M.; Corwin, E. I.; Siemens, A. O.; Brujić, J. A 'Granocentric'model for Random Packing of Jammed Emulsions. *Nature* **2009**, *460*, 611−615.
(64) Lu, X.; Arduini-Schuster, M.; et al. Thermal Conductivity of Monolithic Organic Aerogels. *Science* **1992**, *255*, 971.
(65) Liao, Y.; Wu, X.; Liu, H.; Chen, Y. Thermal Conductivity of Powder Silica Hollow Spheres. *Thermochim. Acta* **2011**, *526*, 178−184.
(66) Notario, B.; Pinto, J.; Solorzano, E.; De Saja, J. A.; Dumon, M.; Rodríguez-Pérez, M. A. Experimental Validation of the Knudsen Effect in Nanocellular Polymeric Foams. *Polymer* **2015**, *56*, 57−67.
(67) Stein, A. Advances in Microporous and Mesoporous Solids—Highlights of Recent Progress. *Adv. Mater.* **2003**, *15*, 763−775.
(68) Wei, G.; Zhang, X.; Yu, F. Thermal Conductivity of Xonotlite Insulation Material. *Int. J. Thermophys.* **2007**, *28*, 1718−1729.
(69) Zhu, Y.; Shi, J.; Shen, W.; Dong, X.; Feng, J.; Ruan, M.; Li, Y. Stimuli-Responsive Controlled Drug Release from a Hollow Mesoporous Silica Sphere/Polyelectrolyte Multilayer Core−Shell Structure. *Angew. Chem.* **2005**, *117*, 5213−5217.
(70) Qiu, C.-W.; Hu, L.; Xu, X.; Feng, Y. Spherical Cloaking with Homogeneous Isotropic Multilayered Structures. *Phys. Rev. E* **2009**, *79*, 047602.
(71) Narayana, S.; Sato, Y. Heat Flux Manipulation with Engineered Thermal Materials. *Phys. Rev. Lett.* **2012**, *108*, 214303.
(72) Maldovan, M. Sound and Heat Revolutions in Phononics. *Nature* **2013**, *503*, 209−217.
(73) Sanders, W.; Gibson, L. Mechanics of Hollow Sphere Foams. *Mater. Sci. Eng., A* **2003**, *347*, 70−85.
(74) Sanders, W.; Gibson, L. Mechanics of Bcc and Fcc Hollow-Sphere Foams. *Mater. Sci. Eng., A* **2003**, *352*, 150−161.
(75) Ashby, M. F.; Johnson, K. *Materials and Design: The Art and Science of Material Selection in Product Design*; Butterworth-Heinemann, 2013.
(76) Wang, L.; Boyce, M. C.; Wen, C. Y.; Thomas, E. L. Plastic Dissipation Mechanisms in Periodic Microframe-Structured Polymers. *Adv. Funct. Mater.* **2009**, *19*, 1343−1350.
(77) Danielsson, M.; Parks, D. M.; Boyce, M. C. Micromechanics, Macromechanics and Constitutive Modeling of the Elasto-Viscoplastic Deformation of Rubber-Toughened Glassy Polymers. *J. Mech. Phys. Solids* **2007**, *55*, 533−561.

DOI: 10.1021/acsaem.7b00264
ACS Appl. Energy Mater. 2018, 1, 1146−1157